Improving Displacement Measurement for Evaluating Longitudinal Road Profiles

Chinedum A. Onuorah, Angus Hutton-Mckenzie, Sara Chaychian, Yichuang Sun, Senior *Member, IEEE*, and Johann Siau

***Abstract*— This paper introduces a Half-Wavelength Peak Matching (HWPM) model, which improves the accuracy of vehicle based longitudinal road profilers used in evaluating road unevenness and mega-textures. In this application, the HWPM model is designed for profilers which utilize a laser displacement sensor with an accelerometer for detecting surface irregularities. The process of converting acceleration to displacement by double integration (which is used in most profilers) is error-prone, and although there are techniques to minimize the effect of this error, this paper proposes a novel approach for improving the generated road profile results. The technique amends the vertical displacement derived from the accelerometer samples, by using data from the laser displacement sensor as a reference. The vehicle based profiler developed for this experiment (which uses the HWPM model) shows a huge improvement in detected longitudinal irregularities when compared with pre-processed results, and uses a 3m rolling straight edge as a benchmark.**

***Index Terms*— Accelerometer, Displacement, Integration error, Laser Displacement Sensor**

I. Introduction

ROAD roughness is a term used to indicate road quality, and this is essential to both vehicle and road maintenance. According to the American Society of Testing and Materials (ASTM), road roughness is "the deviations of a pavement surface from a true planar surface with characteristic dimensions that affect vehicle dynamics, ride quality, dynamic loads, and drainage, for example, longitudinal profile, transverse profile, and cross slope" [1].

The longitudinal road profile is a two-dimensional representation of the road, showing any height/vertical irregularities along a selected path. Road profiling plays an essential part in the maintenance, improvement, and development of road transportation in a general scale, from both point of view of vehicle and road users. From a vehicular standpoint, road surface texture can affect the longevity of parts of the vehicle, as driving on rough and uneven surfaces generate vibrations to the vehicle. Over time, this will have a negative mechanical effect to vehicle parts that make up its unsprung mass, as these are directly affected by the vibrations caused by the road irregularities, especially if this occurs consistently. As a road user, ride comfort and smoothness is the main factor, as this (to an extent) is relative to the vehicle's control and balance during transit.

Autonomous driving has gained considerable interest in recent years as part of the advancements in Intelligent Transport Systems (ITS) [2]–[5]. One major factors in its successful deployment is the ability for these vehicles to correctly interpret road surfaces, since this will allow the autonomous software to react appropriately to the different pavement conditions. The researchers in [6] propose a laser based method of road surface recognition, which detects lane markings and recognizes the surface conditions (i.e. dry, wet etc.) to enable automatic truck platooning.

It is necessary to evaluate longitudinal road profiles, and with the current developments, fast, scalable, and accurate measurement concepts are ideal. Conventional methods of Longitudinal road measurement, use equipment like the rod and level, dipstick, 3m Rolling Straight Edge (RSE), which has a dial in the middle of the frame used to measure vertical irregularities of the road. These are manual processes, and requires a person to be physically present at the location to operate the device and record measurements. More recent concepts employ the use of sensors such as cameras, accelerometers, laser, or a combination of any of these. These sensors are mounted on a vehicle and connected to an on-board computer, which captures and processes samples of the road properties automatically, allowing faster road profiling. These systems usually contain GPS, which is used to tag measured road properties to their respective locations.

A group of researchers [7]–[9] developed models to estimate road surface condition based on data obtained from smartphone sensors. Their work show a linear relationship between the road surface roughness and the vehicle's vertical acceleration. Their goal is to explore easier and low cost methods in road monitoring, and with the increasing popularity and availability of smartphones, considering the presence of the various sensors bundled in them, they provide a viable option in this application. This method is better suited for road texture wavelengths greater than 5m (unevenness) as indicated by Figure 1. This is because the smartphones are typically mounted on the vehicle's dashboard, therefore the range of movement sensed is limited to the allowed frequency range (1 – 4Hz [10]) of the vehicle's sprung mass due to the effect of shock absorbers. Figure 1(a) show the different classifications of road textures, illustrating their respective effect on vehicles and road users. This image is taken from the ISO 13473-5 standard that characterizes pavement textures by

use of surface profiles, where λ and f_{sp} represent the texture wavelength and spatial frequency (cycles/m) respectively. Lighter shades indicate favourable effect of texture over the stated range, where darker shades are unfavourable [11].

For finer texture measurements, other methods like [12] utilize a two dimensional laser displacement sensor to evaluate a three-dimensional road roughness. Guan et al describes an algorithm to automatically detect and extract road features (surface, markings and cracks) from a Mobile Laser Scanning (MLS) point cloud data [13]. In [14], a combination of vision and laser sensors was used, proposing a laser line recognition method that only depends on grey value to determine the roughness, employing an anisotropic diffusion (Perona-Malik) filter to smooth the pavement texture.

Commercially, the combination of both laser and accelerometer sensors is the most widely used method in vehicle mounted profilers, and this is reflected by the services provided by several top pavement testing companies including Highway Data Systems (HDS), PaveTesting, Pavement Management Services (PMS), Oscorp Engineering, Dynatest etc. Where the laser measures the road irregularities (since they can precisely measure displacement, and support high sampling rates), while the accelerometer is used to compensate for the vehicle's vertical displacement during transit. An accelerometer is better suited for measuring the vehicle dynamics in this application since they do not require a physical reference point as lasers do, because the evaluated displacement is relative to its previous position. As an example, if the vehicle drives over a hump, the true road profile, for the period where the tires are over the hump, will be the difference between the displacement measured by the laser (from mount position to the ground) and the vertical (z-axis) displacement measured from the accelerometer (which is calculated by double integration of the acceleration samples). Yang et al shows an implementation of this system, which utilises two accelerometers and a laser displacement sensor mounted in front of a vehicle [15]. The advantage with this method is, the road texture wavelength measureable is a factor of the speed of the vehicle and the sampling rate of the laser displacement sensor. Hence, in theory road textures as low as 0.5mm can be evaluated.

One of the challenges with these systems is being able to precisely derive the vertical displacement from the accelerometer, since the integration process during conversion amplifies any slight error measured by the accelerometer. The presence of a low frequency or DC signals causes the evaluated displacement waveform to drift away from the expected result. This drift is due to the integration process of converting the acceleration samples to displacement, and the most common method of reducing this error is by passing the derived displacement through a high-pass filter, to eliminate low frequency signals present. The concept of utilizing Inertial Measurement Unit (IMU) sensors (which typically consists of an accelerometer and gyroscope) in motion applications to detect the movement of a body is common practice. Do et al proposes an inverted pendulum model [16] that evaluates the vertical displacement derived from an accelerometer (mounted at the upper torso), to detect a person's step, and estimating the stride length for infrastructureless localization. Similarly, the researchers in [17], [18] integrate IMU sensors with Global Positioning System (GPS) signals to improve localization accuracy in areas where GPS signals are unavailable.

The works carried out by the researchers in [19]–[25] confirm the negative effect of drift in applications that use IMU sensors to derive displacement. Various solutions were proposed in these studies to minimize the effect of this drift in their respective applications. For applications that require precise displacement calculations like in [20], [25] where an IMU sensors is used to detect an object's physical position, by computing the displacement from its initial location, Kalman filters are typically used. This technique works by estimating an error offset on the evaluated displacement, based on a mathematical model that integrates the measurements obtained from other related sensors. The correction models in [19], [21] are targeted to applications where the motion of the object is periodic, and its theory basically relies on pre-existing knowledge of the expected frequencies or band.

This paper proposes a model based on a peak matching principle, that is applied to the displacement waveform derived from the accelerometer. This model compares the accelerometer's displacement with that of the laser sensor, and then calculates a correction offset. This offset value is then subtracted from the accelerometer's displacement, reducing the errors added to the signal during the integration process, thereby improving the accuracy of the overall system.

Table 1, extracted from the Series 700 Road Pavement Standard [26], highlights the significance of this correction model for vehicle-based road measurement systems that combines accelerometers with displacement sensors to evaluate surface irregularities. There are two longitudinal threshold heights (4mm and 7mm), with their respective acceptable tolerances used to determine the eligibility of the road. From the standard, irregularities exceeding 10mm have zero tolerance, and is not permitted.

II. System Setup and Design

The Data Acquisition (DA) device used was designed and developed by the researchers of this project at component level by utilising commercially available sensors to achieve the required functionality. This DA system consists of an accelerometer (MPU-9250), a single point laser displacement sensor (optoNCDT 1700), and a Doppler radar (PEGASEM GSS15). The accelerometer is used to monitor the vertical displacement of the vehicle, the laser sensor measures the distance between the device's mount position on the vehicle to the road surface, while the Doppler radar estimates the vehicle speed. All operations of the DA device are handled by a LPC1768 Microcontroller which runs a custom firmware. The firmware defines the operations of the system, exposing a platform for communication and control, acting as a bridge to interact with the integrated sensors. This device communicates with a computer over a Local Area Network (LAN), and is powered via Power Over Ethernet (POE). Figure 2 shows a

block level diagram of the system's assembly.

During road surface measurement, the device is mounted at the back of the vehicle and aligned to the right rear tire as shown in Figure 3. The project focuses at analyzing road surface conditions affecting vehicle wear and discomfort to travelers, which covers the texture wavelengths between 50mm - 50m as shown in Figure 1a. The main factors that determine the road texture wavelength measureable by the DA device are the sensor's sampling rates and vehicle speed. In terms of sampling rate, since the laser displacement sensor measures the actual road surface irregularities, its sampling rate has the most direct effect on the measureable texture wavelength, and hence, determines the overall sampling rate used by the DA unit. To measure smaller road texture wavelengths, a higher laser sampling rate and lower vehicle speed is required.

The decision on the sampling rate and vehicle speed was chosen based on parameters that will yield a scalable and accurate analysis of the desired road texture. This includes considerations on the size of data that is generated by the DA device, without compromising the evaluated profile accuracy. For the results shown in this paper, a sampling rate of 625Hz was used, at vehicle speeds from 20mph to 50mph, which allows for road texture measurement within 14mm – 22m wavelength range (using equation (1)).

$$Measurement\ range = v * \frac{n}{fs} \quad (1)$$

Where $\boldsymbol{v}$ is the vehicle speed, $\boldsymbol{fs}$ is the sampling rate, and $\{\boldsymbol{n} \in \mathbb{R} \mid 1 \leq \boldsymbol{n} \leq fs\}$, which is used to calculate the possible measurement range where a value of $\boldsymbol{n} = \mathbf{1}$ and $\boldsymbol{n} = \boldsymbol{fs}$ are the minimum and maximum road textures that can be evaluated.

Before applying the correction model, samples from the accelerometer must be converted to displacement by double integration. The derived accelerometer displacement (dA) and laser displacement (dL) must be high pass filtered to eliminate any DC or low frequency signals that may be present in the data to minimize the error. For this application, a cut-off frequency of 1Hz was chosen, which corresponds to the natural frequency (1 – 4Hz [10]) of a car's sprung mass (part of the vehicle supported by the suspension). This is also reflected in Figure 4, which shows measured dL samples (obtained using the DA device) in the frequency domain.

Note that all graphs showing dA and dL samples in this paper are actual road measurements taken with the DA device.

The laser sensor shows the presence of a single frequency band between 0 < f < 4Hz, as opposed to the acceleration (z-axis) samples which shows three different bands (A, B and C). The common band 'A' between the laser and accelerometer samples correlate with the natural frequency of the vehicle's sprung mass. This frequency reflects the vertical dynamics of the vehicle supported by the suspension system while in motion. Bands B and C are a result of higher frequency vibrations acting on the chassis, caused by a combination of engine and mechanical vibrations. This is verified by comparing the samples obtained while the vehicle is static (with engine running), with samples obtained while the vehicle is in motion. The focus for this application is on band A, as the goal is to detect and subtract the vehicle's vertical dynamics from the laser's measurement samples when in motion. A low pass filter is applied to the acceleration samples to remove frequencies greater than band A.

III. Half-wavelength Peak Matching (HWPM) Model

The HWPM model compares and matches the peak amplitudes of two signals, where one acts as a reference, and the other is the signal to be corrected. The laser displacement sensor used operates on the principle of optical triangulation, where a visible point of light is projected on a surface from a light source, and an image receiver positioned at a pre-defined angle captures the reflection of the light spot, then calculates the distance between the visible spot and its projection source. This is a high precision sensor with error margins of ±0.25% (as stated in the optoNCDT 1700 datasheet). Since the measurement from the laser is expected to be more precise, it is better suited as the reference when compared to the displacement values derived from the accelerometer.

Figure 5 shows the longitudinal profile estimation obtained before applying the HWPM model. At this stage, the displacement signals have been high-pass filtered at a cut-off frequency of 1Hz. Analysing the graph, there are clear similarities in the low frequency characteristics of both the laser and accelerometer samples. This is made clearer after both samples are low pass filtered (fc = 2Hz) to remove the high frequency components of the waveforms. This also exposes the error present in the dA waveform, where the low frequency displacement peaks appear higher than that of the dL as shown in Figure 6.

Using a hump as an example, considering the mount position of the DA device (behind vehicle, aligned to left tire), for the period where the front tires climb over the hump, theoretically, both dA and dL record the same low frequency amplitudes caused by the back of the vehicle swinging down and up in the opposite direction of the front tires, as they climb up and down from the hump. This is a similar feature shown when the dampers on the vehicle balances the car after being displaced vertically because of road irregularities. The difference between dA and dL is expected to occur from the moments when the rear tires of the vehicle climb over the hump, to the laser sensor hovering over the hump. There is a phase difference on the signals at this point. While the dA maintains the absolute displacement of the DA device for the period where the rear tires climb over the hump, the laser sensor begins to record a dip in measurement since it hovers over the hump.

Depending on the distance between the midpoint of the rear tires and the mount position of the DA device, this dip is reflected before or after the period where the dA begins to descend.

In most cases, there is a direct correlation between the phase and peak amplitude of both dA and dL signals, however, as

the phase between the signals begin to drift apart, the difference in peak amplitudes for the same periods increases. Since little to no change is expected in the peak amplitudes of both dA and dL signals at periods where they are both in phase, the HWPM model detects and corrects this difference. The HWPM model implementation is done in three phases, as described below:

1. Peak Detection and Classification
2. Peak Matching
3. Edge Smoothing.

A. Peak Detection and Classification

The aim of this stage in the correction technique is to identify all Common Peaks (CPs) present between the dA and dL signals. Peaks P1, P2, and P3 in Figure 6 are examples of these common peaks. These are essentially peaks (with the same polarity) present in both dA and dL waveform for any given wavelength, signifying correlation between the signals. Peaks P4 show peaks that are present in the dL signal but not on the dA, these will be referred to as uncommon peaks (UPs). The same goes for peaks that may be present in dA signal but not on the dL.

There were two methods considered for identifying the peaks in the signal. The first method uses a Difference in Gradient Polarity (DGP) peak estimation process, which is ideal for low frequency signals, as it simply identifies peaks based on a difference in gradient polarity between the samples. Algorithm 1 shows an implementation of this method, the process sequentially runs through all the samples, calculating the gradient (equation

(2)) between two subsequent samples, and comparing each one with previously calculated gradient. Peaks are detected at points when equation (3) is true, when the polarity of a gradient is different to its predecessor i.e. polarity of $\boldsymbol{m_{n-1}}$ is not equal to polarity of $\boldsymbol{m_n}$. The output of the algorithm is a buffer with a length equal to the number of samples. The buffer contains a value of +1 or -1 at sample locations to represent a positive or negative peak respectively, otherwise the value is 0.

$$m_n = \frac{\Delta y}{\Delta x} \tag{2}$$

$$sign\ (m_{n-1}) \neq sign(m_n) \tag{3}$$

Where $\boldsymbol{m_n}$ is the gradient, $\boldsymbol{m_{n-1}}$ is the previous gradient, $\boldsymbol{\Delta y}$ is the difference between the samples, and $\boldsymbol{\Delta x}$ is the change on the x-axis, which will always have a value of 1 in this case, since the comparison is done between two subsequent samples, hence:

$$m_n = \Delta y \tag{4}$$

The other method considered was the Zero Threshold (ZT) peak estimation, which identifies peaks based on finding the maximum/minimum sample value between two subsequent points where the signal is at zero.

There is a flaw with this technique especially in this application. Since the peak is identified based on the zero threshold, a signal containing peaks as shown in P5 (i.e. peaks that do not intersect with the x-axis zero threshold) will be missed by this method of estimation. Therefore, the DGP technique was preferred for this test.

Algorithm 2 identifies the CPs in the signal, which is the focus of the HWPM model as mentioned earlier in the literature, as UPs suggests actual road irregularities and should not be corrected. With this DGP technique, it is expected that two consecutive peaks in a signal cannot be of the same polarity, since a peak can only be identified as a difference in gradient polarity. The output of the algorithm is two Lists containing the values of the identified common peaks for both dL and dA signals at the same index.

Algorithm 1 Pseudocode for DGP peak detection

```
1.  Initialise 'output_buffer' with values equal to 0
2.  FOR EACH sample S in 'input_buffer'
3.      calculate current gradient using previous sample
4.      IF current polarity is not equal to previous polarity
5.          IF current gradient is greater than or equal to 0
6.              set value at index of 'output_buffer' to -1
7.          ELSE
8.              set value at index of 'output_buffer' to 1
9.      update previous gradient equal to current gradient
```

Algorithm 2 Pseudocode for CP classification

```
1.  FOR EACH sample A and B in 'buf_A' and 'buf_B'
2.      IF A is not equal to 0
3.          set 'pkA_temp' equal to A
4.          IF 'pkA_temp' is equal to 'pkB_temp'
5.              add 'pkA_temp' to 'CP_buffer_A'
6.              add 'pkB_temp' to 'CP_buffer_B'
7.      IF B is not equal to 0
8.          set 'pkB_temp' equal to B
9.          IF 'pkB_temp is equal to 'pkA_temp
10.             add 'pkB_temp' to 'CP_buffer_B'
11.             add 'pkA_temp' to 'CP_buffer_A'
```

B. Peak Matching

After detecting the peaks, the next phase is to apply the peak matching technique on the necessary sections of the waveform, ignoring areas where the peak appears on only one of the signals i.e. UPs. The peak matching is done in half wavelengths on the perimeter of either side of the peak point, as shown in Figure 7.

For regular periodic signals, this process can be done by calculating the wavelength of one cycle of the signal, and performing the peak matching process at set intervals on half of the calculated wavelength. But from the wave sample shown in Figure 7, using this approach will result in false calculations because the actual dA and dL waveforms are not

periodic, and they contain multiple signals with multiple wavelengths.

Therefore, the method employed in this model calculates the midpoint between each peak using equations

(5) and (6) on the dA waveform to detect a quarter wavelength on either side of the peak. Both quarter wavelengths form the half wavelength to be corrected from the peak, and results obtained using this approach show accurate correction values.

$$LM = \left\lfloor \frac{x(t)_p + x(t)_{p-1}}{2} \right\rfloor \quad (5)$$

$$RM = \left\lfloor \frac{x(t)_{p+1} + x(t)_p}{2} \right\rfloor \quad (6)$$

Where $\boldsymbol{LM}$ is the midpoint to the left of peak (point A in Figure 7), $\boldsymbol{RM}$ is the midpoint to the right of peak (point B in Figure 7), $\boldsymbol{x(t)_p}$ is the current peak's x-axis index, $\boldsymbol{x(t)_{p-1}}$ is the previous peak's value to the left of $\boldsymbol{x(t)_p}$, and $\boldsymbol{x(t)_{p+1}}$ is the next peak's value to the right of $\boldsymbol{x(t)_p}$.

After calculating the length for the half wavelength, equation

(7) is used to determine the offset that needs to be subtracted from each data point in the signal to correct it.

$$offset = ya_{min} + \frac{(yb_{max} - yb_{min}) * (ya(t) - ya_{min})}{(ya_{max} - ya_{min})} \quad (7)$$

Where $\boldsymbol{ya(t)}$ is the amplitude of the dA signal with respect to time, $\boldsymbol{ya_{min}}$ is the minimum value of the dA signal's quarter wavelength, $\boldsymbol{ya_{max}}$ is the maximum value of the dA signal's quarter wavelength, $\boldsymbol{yb_{max}}$ is the maximum value the dA signal can be scaled to (higher value between the dL's peak and dA's highest amplitude), and $\boldsymbol{yb_{min}}$ is the minimum value the dA signal can be scaled to (lower value between the dL's peak and dA's lowest amplitude).

C. Edge Smoothing

The peak matching process causes discontinuity on the waveform as shown in Figure 8, which primarily occurs at the mid-points between the peaks. This is expected since the scale factor for each half wavelength is only dependent on its CP difference, hence, the midpoint at which they join show features of discontinuity. The purpose of this part of the algorithm is to eliminate this property, giving the waveform a smooth transition between the corrected half wavelengths. The edge smoothing is accomplished using a low pass filter with an acceptable cut-off frequency ($\boldsymbol{f_c}$= 4Hz).

IV. Results

As illustrated in Figure 9, the HWPM model corrects any amplitude error offset imposed on the dA signal. As shown, the process adjusts the peaks in the dA signal to match that of the dL, while maintaining the overall shape of the wave form and the phase difference between them. For the results shown, MATLAB was used to implement the HWPM model and perform all related analysis on the measured samples.

A. Effect of a high-pass filter

As the cutoff frequency is increased, dA becomes identical to dL, because the filter eliminates more of the drift in dA, as shown in Figure 10. There is a limit to this increment, because the amplitude of the signals is attenuated at higher cutoff frequencies, hence, losing useful information as indicated in Figure 10 (d). The cutoff frequency is based on the required road texture wavelength. Assuming a road texture wavelength of 10m, for a vehicle speed of 20m/s (45mph) the frequency of the texture wavelength is 2Hz. Therefore, the high-pass cutoff frequency should not exceed this value.

B. Effect of speed on the high-pass cutoff frequencies

Results gathered for the experiment suggests that the speed of the vehicle influences the amount of drift imposed on the dA signal after double integration. This is a direct relationship where the drift increases with speed, and requires a higher cutoff frequency from the high pass filter to eliminate it.

Figure 11 illustrates this theory. Comparing the waveforms obtained at the different speeds, the drift on the dA signal increases progressively as the speed rises from 20mph to 50mph, and this is more evident when the cutoff frequency is at 0.1Hz. This is mainly due to the difference in wavelengths occurring at these speeds. Ultimately, the frequency sensed by the vehicle chassis is limited because of the dampers, and although this frequency range is consistent, the equivalent wavelength changes because it is dependent on the speed of the vehicle. On the waveform, a wavelength with a frequency of 1Hz will have an equivalent travel distance of 8.9m at a vehicle speed of 20mph (8.9m/s), and 22.4m when the vehicle is travelling at 50mph (22.3m/s). The low frequency component of the waveform equates to a larger distance at higher speeds, hence, the increase in drift after integration.

C. Effect of HWPM on drift

The plots (Figure 12 and Figure 13) demonstrates the purpose of the HWPM algorithm in correcting drift in the dA signal. The samples were obtained for two different speeds at 20mph and 50mph respectively. Each image has two sets of data (separated by a column) showing the result of the evaluated dA waveform before and after applying the HWPM algorithm. Note that the profile samples were taken at different locations. As the cutoff frequency increases, the dA waveform becomes progressively equivalent to its dL counterpart irrespective of the HWPM. However, comparing both sets of results for the various speeds, better drift correction is achieved with the HWPM. Without the HWPM, a cutoff frequency of at least 1Hz is typically required to sufficiently eliminate any drifts in the waveform (as shown in the plots), especially in higher vehicle speeds. Whereas, with the HWPM the same level of drift elimination is achieved at half (50%) the cutoff frequency. The HWPM reduces the amount of low frequency signal that is ignored by the high pass filter that could potentially contain useful profiling

information.

This is better observed in low speed conditions. Figure 14 shows this data loss, where the vehicle is used to sample a road hump at 10mph. Comparing the waveforms in the image, there is a significant change at 'x' which depicts the hump. As the cutoff frequency increases, the filter progressively alters the representation of the hump. This is because the hump produces a very low frequency signal, which is increasingly ignored by the filter, as the cutoff frequency gets higher. Since the laser signal is used as the reference for the HWPM algorithm in this application, it is vital to maintain the originality of this reference signal as best as possible, because inaccuracies are translated to the active signal in HWPM.

For laser based road profilers, it is important to select an appropriate high pass cutoff frequency for the dA signal. Because of the longitudinal irregularity thresholds defined in the series 700 road pavement standard (Table 1), an incorrect cutoff frequency could cause a pavement to be evaluated above or below the outlined thresholds.

D. Comparing the evaluated road profile against a 3m Rolling Straight Edge

Figure 15 shows the effect of the HWPM model on the results in terms of irregularities measurements, and the results are based on running a 12cm diameter wheel filter over the original dA samples to simulate a Rolling Straight Edge (RSE). The laser sensor has a light spot diameter of approximately 1mm, compared to a RSE which uses a wheel to measure the road longitudinal displacements. The purpose of the wheel filter is to imitate the effect of the RSE wheel over the laser samples, and this is done with a moving average filter.

Over the 300m distance analysed for the test, using a 3m rolling straight edge, the device measured a total of 9 irregularities on the 4mm scale. Before applying the HWPM model, 19 irregularities were detected on the 4mm scale. Applying the technique brought the measured number of irregularities to 6. Using the data obtained from the RSE as a benchmark, the results obtained before and after the HWPM correction model indicates about 70% improvement on the 4mm scale (from 19 to 6 respectively), which is significant considering the analysis is done based on the maximum permitted number of surface irregularities on each scale. No irregularity was measured on the 7mm and 10mm scale for all three cases.

V. Conclusion

Vehicle-based rapid road profiling has become a popular concept in road analysis because of its speed, as opposed to more traditional methods like 3m rolling straight edge. Although traditional methods of road measurements are still very much in use, as they offer better accuracy and are relatively cheaper, steps are being taken to improve vehicle-based methods as there is still room for improving its accuracy. The proposed HWPM correction model shows significant improvements (~ 70%) to laser based vehicle profilers, by using an amplitude matching technique to adjust the offset displacement derived from the accelerometer.

There is still room for improvement of this algorithm. As it is, the HWPM model does not consider any phase difference between each half wavelength during the correction process. Brief investigations made on this suggests there is an effect on the dA signal's amplitude, caused by a phase difference with the dL signal. Further analysis will be carried out to verify this evidence.

References

[1] ASTM E867-06(2012), "Standard Terminology Relating to Vehicle-Pavement Systems," 2012.

[2] L. Hobert, A. Festag, I. Llatser, L. Altomare, F. Visintainer, and A. Kovacs, "Enhancements of V2X communication in support of cooperative autonomous driving," *IEEE Communications Magazine*, vol. 53, no. 12. pp. 64–70, 2015.

[3] I. Pettersson and I. C. M. Karlsson, "Setting the stage for autonomous cars: a pilot study of future autonomous driving experiences," *IET Intelligent Transport Systems*, vol. 9, no. 7. pp. 694–701, 2015.

[4] B. Okumura, M. R. James, Y. Kanzawa, M. Derry, K. Sakai, T. Nishi, and D. Prokhorov, "Challenges in Perception and Decision Making for Intelligent Automotive Vehicles: A Case Study," *IEEE Transactions on Intelligent Vehicles*, vol. 1, no. 1. pp. 20–32, 2016.

[5] C. H. Fleming and N. G. Leveson, "Early Concept Development and Safety Analysis of Future Transportation Systems," *IEEE Transactions on Intelligent Transportation Systems*, vol. 17, no. 12. pp. 3512–3523, 2016.

[6] M. Aki, T. Rojanaarpa, K. Nakano, Y. Suda, N. Takasuka, T. Isogai, and T. Kawai, "Road Surface Recognition Using Laser Radar for Automatic Platooning," *IEEE Transactions on Intelligent Transportation Systems*, vol. 17, no. 10. pp. 2800–2810, 2016.

[7] G. Alessandroni, A. Carini, and L. Emanuele, "Sensing road roughness via mobile devices: A study on speed influence," *2015 9th Int. Symp. Image Signal Process. Anal.*, pp. 270–275, 2015.

[8] V. Douangphachanh and H. Oneyama, "Formulation of a simple model to estimate road surface roughness condition from Android smartphone sensors," *2014 IEEE Ninth Int. Conf. Intell. Sensors, Sens. Networks Inf. Process.*, pp. 1–6, 2014.

[9] H. P. M. and V. P. Gopi, "Vehicle Vibration Signal Processing for Road Surface Monitoring," *IEEE Sensors Journal*, vol. 17, no. 16. pp. 5192–5197, 2017.

[10] Y. J. Wong, "Theory of Ground Vehicles," 4th ed., JOHN WILEY & SONS, 2008, p. 592.

[11] ISO, "ISO 13473-5:2009 Characterization of pavement texture by use of surface profiles — Part 5: Determination of megatexture," p. 29, 2009.

[12] X. Zhu, Y. Chen, Y. Liu, and D. Liu, "Three-Dimensional Road Roughness Measurement System Development Based on Laser Rangefinder," *2015 International Conference on Computational Intelligence and Communication Networks (CICN)*. pp. 1613–1616, 2015.

[13] H. Guan, J. Li, Y. Yu, M. Chapman, and C. Wang, "Automated Road Information Extraction From Mobile Laser Scanning Data," *IEEE Transactions on Intelligent Transportation Systems*, vol. 16, no. 1. pp. 194–205, 2015.

[14] Z. Yuan, X. Zhang, S. Liu, X. Han, and Y. Du, "Laser line recognition for autonomous road roughness measurement," *2015 IEEE International Conference on Cyber Technology in Automation, Control, and Intelligent Systems (CYBER)*. pp. 436–440, 2015.

[15] D. Yang, Y. Han, and X. Lian, "Research on rapid measurement of medium short wave longitudinal road profiles," *Proc. - Int. Conf. Electr. Control Eng. ICECE 2010*, vol. 1, pp. 1742–1745, 2010.

[16] T. N. Do, R. Liu, C. Yuen, M. Zhang, and U. X. Tan, "Personal Dead Reckoning Using IMU Mounted on Upper Torso and Inverted Pendulum Model," *IEEE Sensors Journal*, vol. 16, no. 21. pp. 7600–7608, 2016.

[17] A. Suprem, V. Deep, and T. Elarabi, "Orientation and Displacement Detection for Smartphone Device Based IMUs," *IEEE Access*, vol.

5. pp. 987–997, 2017.
[18] S. Zihajehzadeh, T. J. Lee, J. K. Lee, R. Hoskinson, and E. J. Park, "Integration of MEMS Inertial and Pressure Sensors for Vertical Trajectory Determination," *IEEE Transactions on Instrumentation and Measurement*, vol. 64, no. 3. pp. 804–814, 2015.
[19] N. Millor, P. Lecumberri, M. Gómez, A. Martínez-Ramírez, and M. Izquierdo, "Drift-Free Position Estimation for Periodic Movements Using Inertial Units," *IEEE Journal of Biomedical and Health Informatics*, vol. 18, no. 4. pp. 1131–1137, 2014.
[20] H. Zhao and Z. Wang, "Motion Measurement Using Inertial Sensors, Ultrasonic Sensors, and Magnetometers With Extended Kalman Filter for Data Fusion," *IEEE Sensors Journal*, vol. 12, no. 5. pp. 943–953, 2012.
[21] U. X. Tan, K. C. Veluvolu, W. T. Latt, C. Y. Shee, C. N. Riviere, and W. T. Ang, "Estimating Displacement of Periodic Motion With Inertial Sensors," *IEEE Sensors Journal*, vol. 8, no. 8. pp. 1385–1388, 2008.
[22] Y. Stebler, S. Guerrier, and J. Skaloud, "An Approach for Observing and Modeling Errors in MEMS-Based Inertial Sensors Under Vehicle Dynamic," *IEEE Transactions on Instrumentation and Measurement*, vol. 64, no. 11. pp. 2926–2936, 2015.
[23] H. Ahmed and M. Tahir, "Accurate Attitude Estimation of a Moving Land Vehicle Using Low-Cost MEMS IMU Sensors," *IEEE Transactions on Intelligent Transportation Systems*, vol. 18, no. 7. pp. 1723–1739, 2017.
[24] Z. W. Wu, M. L. Yao, H. G. Ma, and W. M. Jia, "De-noising MEMS inertial sensors for lowcost vehicular attitude estimation based on singular spectrum analysis and independent component analysis," *Electronics Letters*, vol. 49, no. 14. pp. 892–893, 2013.
[25] R. Ferrero, F. Gandino, M. Hemmatpour, B. Montrucchio, and M. Rebaudengo, "Exploiting Accelerometers to Estimate Displacement," *5th Mediterr. Conf. Embed. Comput. 2016*, pp. 206–210, 2016.
[26] HA, "Volume 1 Series 700 Road Pavements -General," 2016.

Table 1
MAXIMUM PERMITTED NUMBER OF SURFACE IRREGULARITIES [26].

	Surfaces of each lane of carriageway, each hard strip and each hard shoulder for each irregularity limit				**Surfaces of each lane of bituminous binder courses for carriageway, hard strip and hard shoulder for each irregularity limit**				**Surfaces of lay-bys, service areas, and associated bituminous binder courses for each irregularity limit**			
Irregularity Limits	4 mm		7 mm		4 mm		7 mm		4 mm		7 mm	
Length (m)	300	75	300	75	300	75	300	75	300	75	300	75
Category A* Roads	20	9	2	1	40	18	4	2	40	18	4	2
Category B* Roads	40	18	4	2	60	27	6	3	60	27	6	3

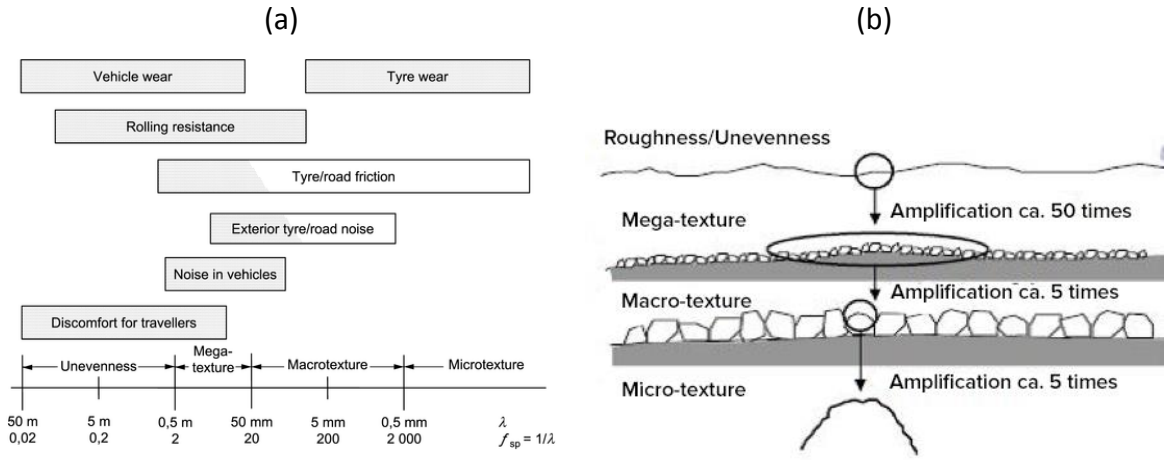

Figure 1: Road texture classifications and visualization [11]

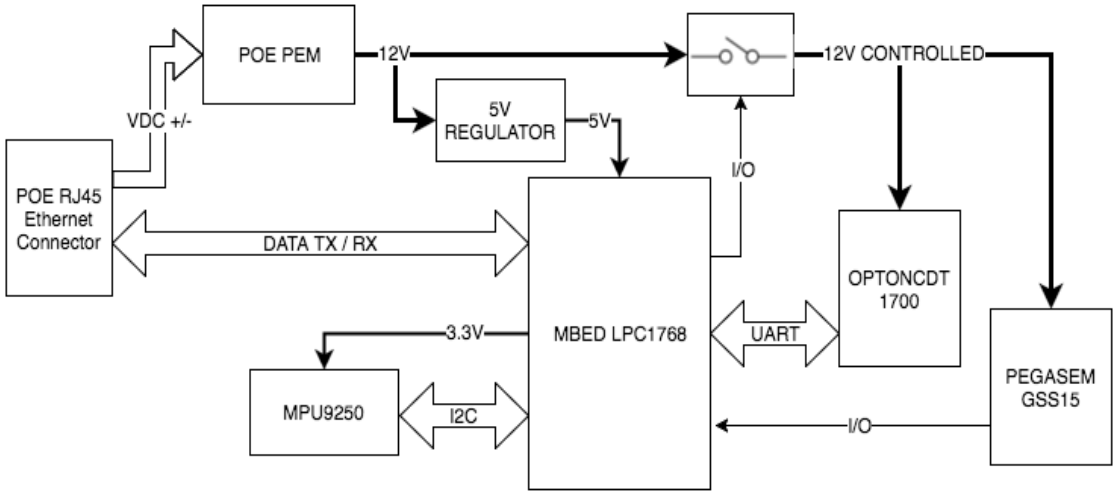

Figure 2: Block diagram of DA device

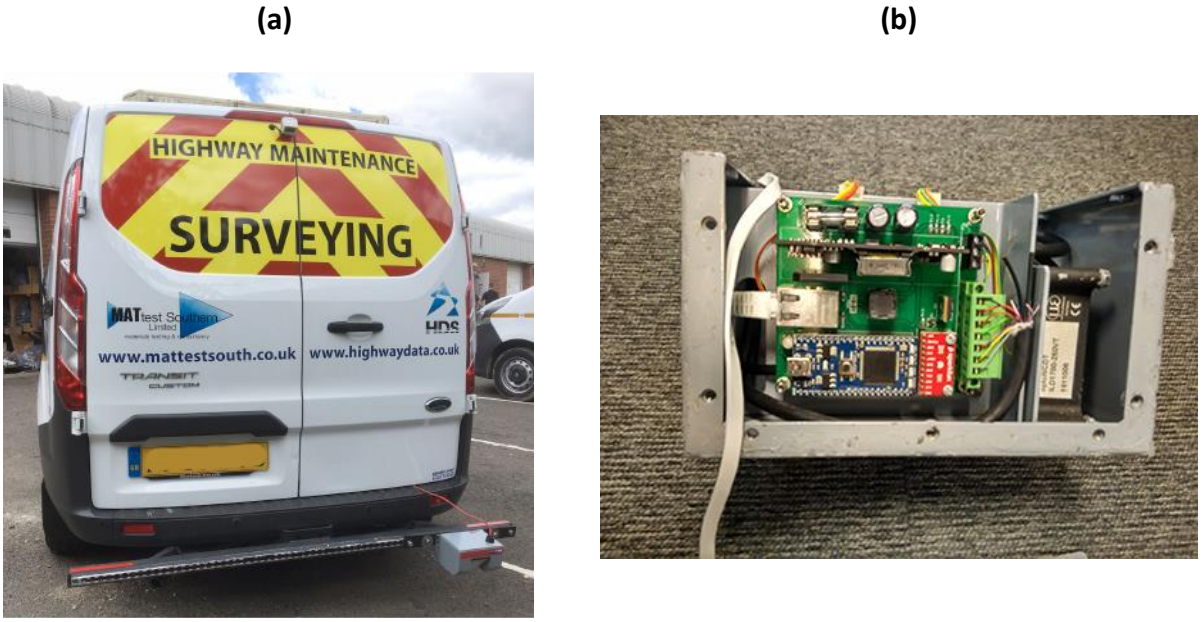

Figure 3: Data acquisition hardware. (a): mount location, (b): internal circuitry

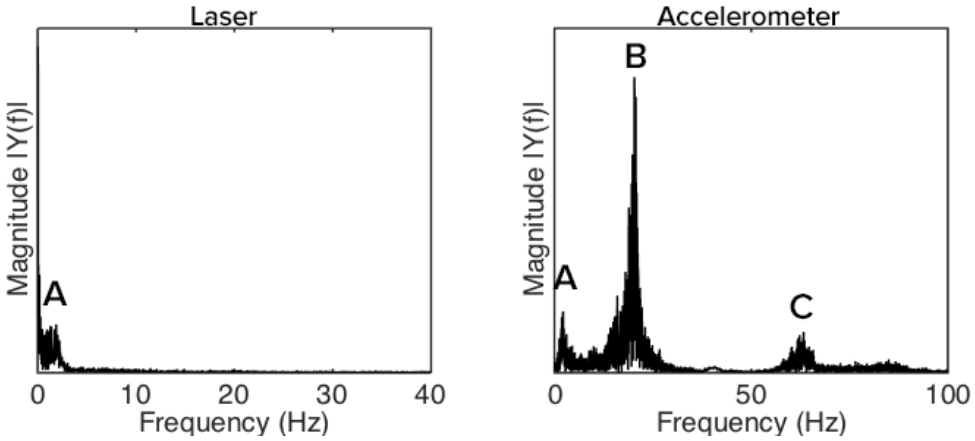

Figure 4: Frequency domain of laser and accelerometer samples.

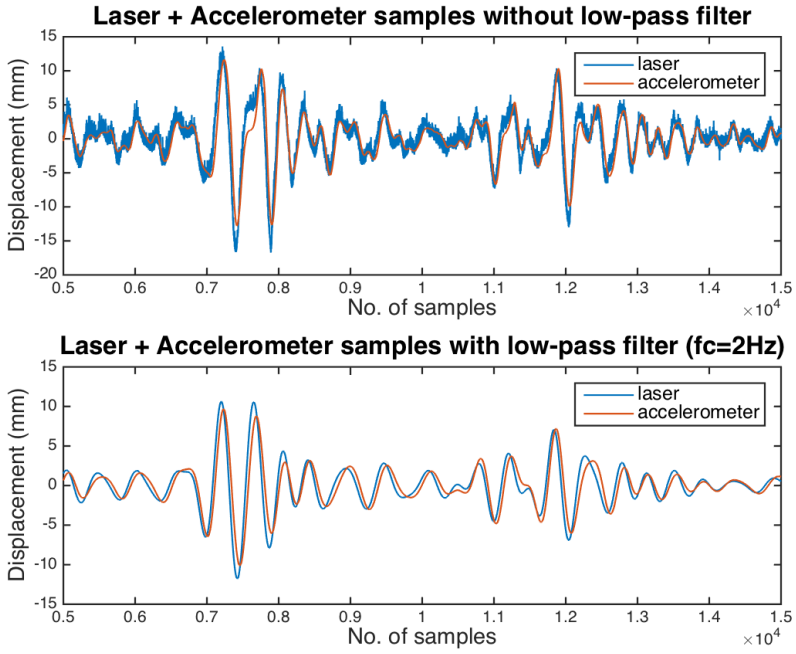

Figure 5: Laser and accelerometer displacement waveforms before and after low pass filtering (f_c=2Hz).

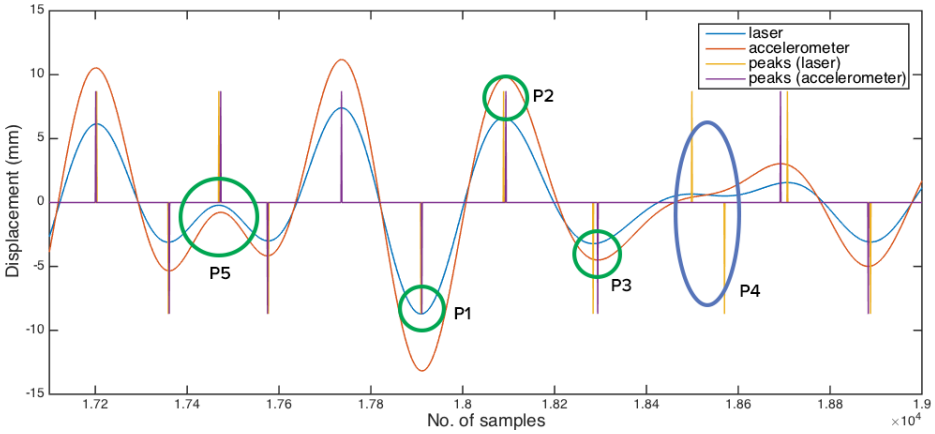

Figure 6: Peak identification using DGP estimation, showing the difference between CPs and UPs.

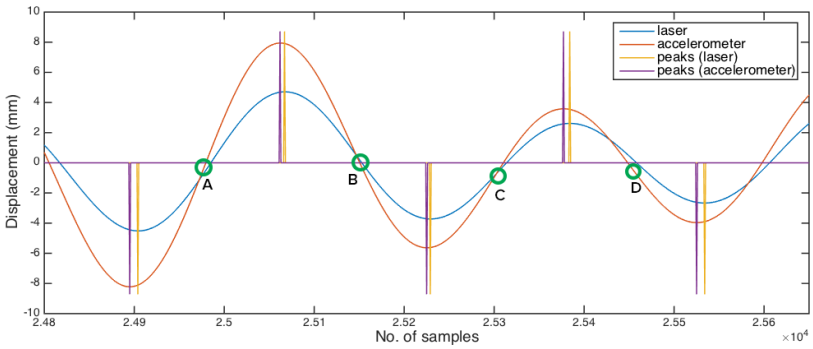

Figure 7: Laser and accelerometer samples, showing the half wavelength peak matching points between successive CPs.

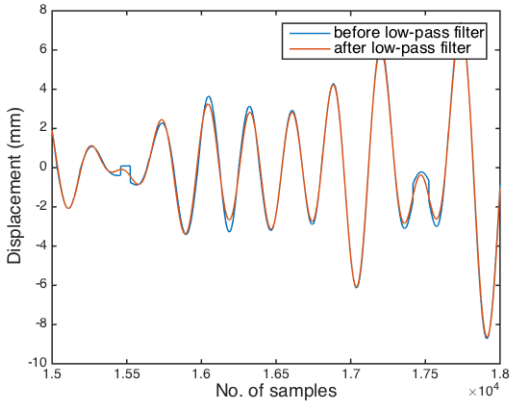

Figure 8: Effect of applying a low pass filter for edge smoothing.

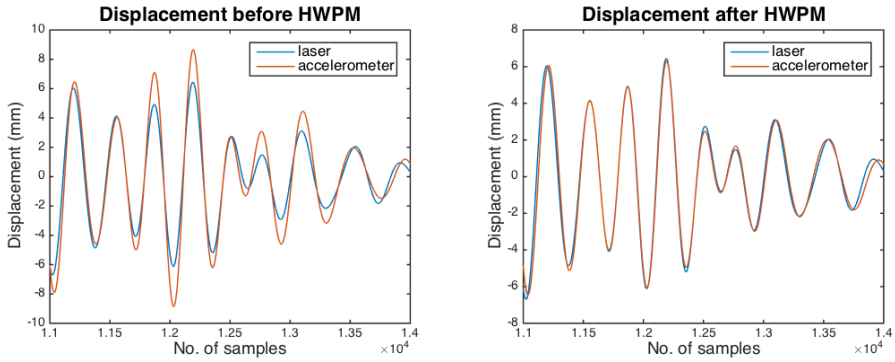

Figure 9: dA and dL signal before and after applying the HWPM.

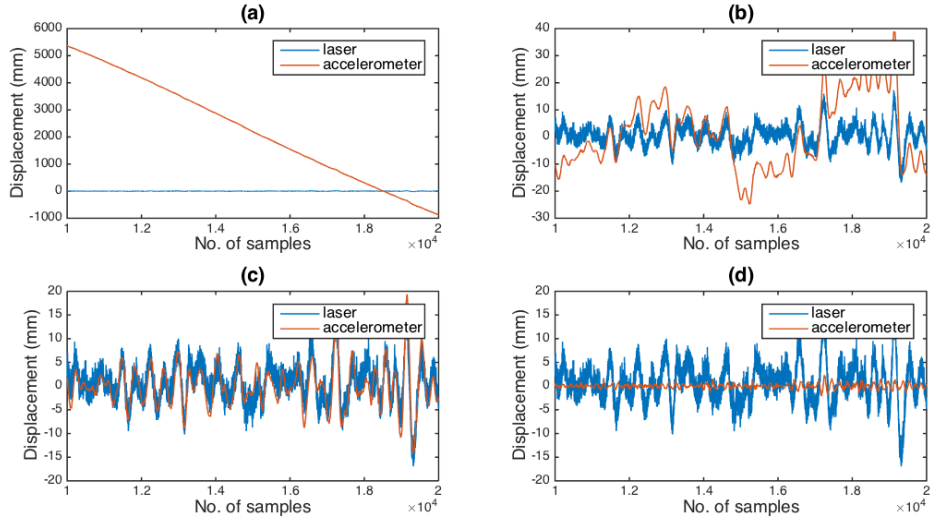

Figure 10: Comparing dA and dL at different cut-off frequencies. (a): fc = 0Hz, (b): fc = 0.3Hz, (c): fc = 1Hz, (d): fc = 2Hz

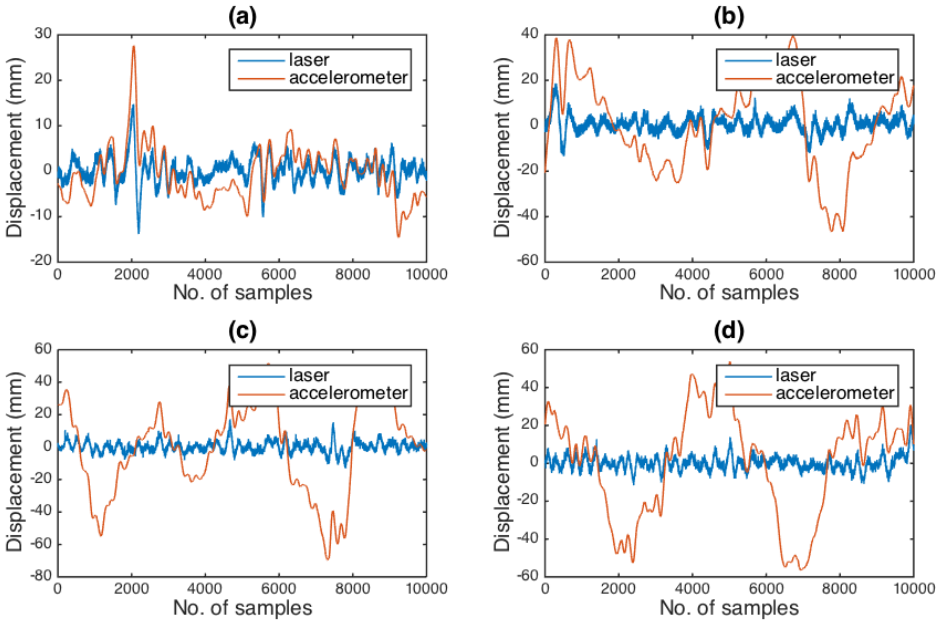

Figure 11: dL and dA samples high pass filtered with a cut-off frequency of 0.1Hz, showing the effect of speed on the dA drift. (a) v = 20mph, (b) v = 30mph, (c) v = 40mph, (d) v = 50mph.

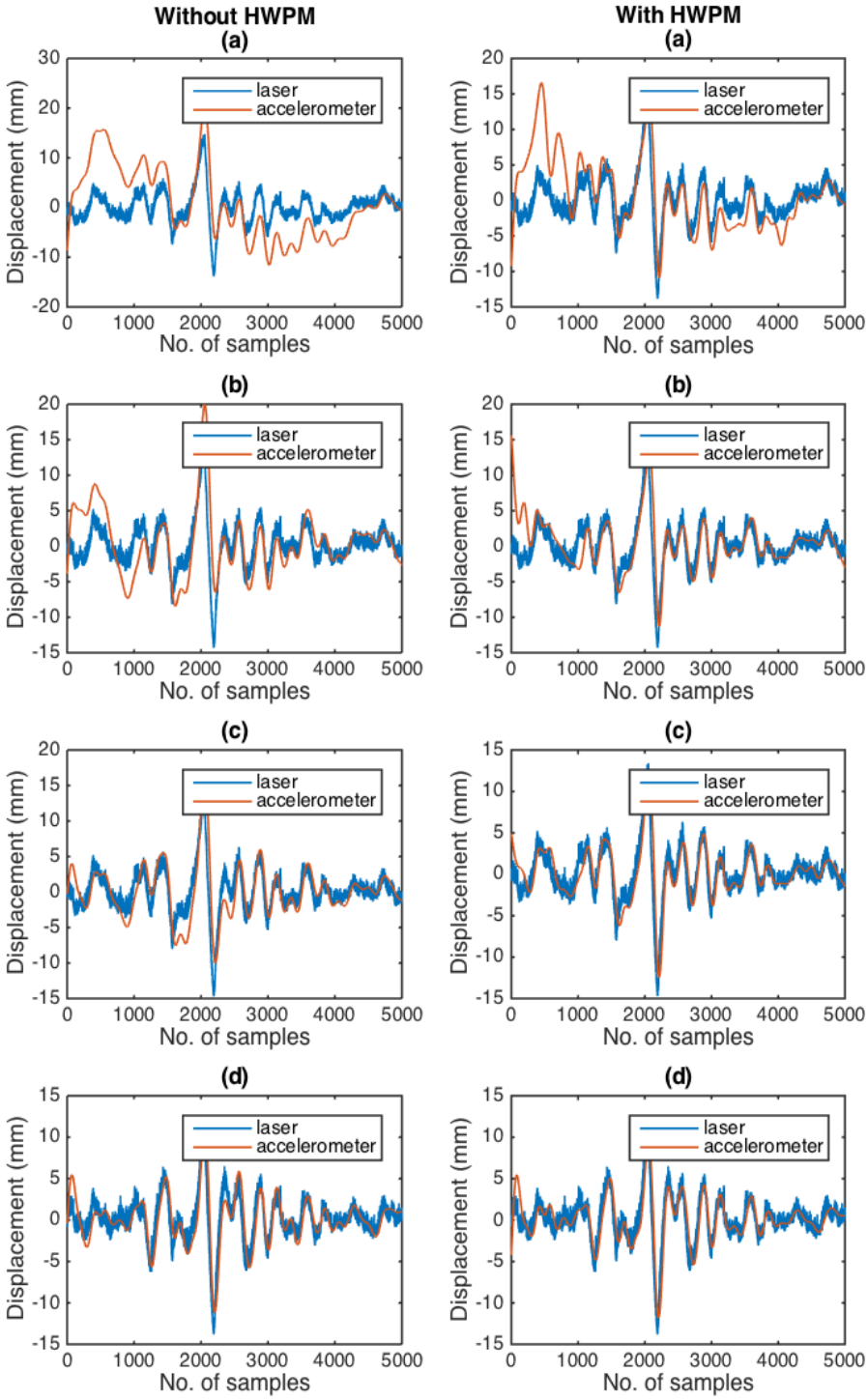

Figure 12: dL and dA samples measured at 20mph to evaluate the drift correction done by HWPM at different cut-off frequencies. (a) fc = 0.1Hz, (b) fc = 0.3Hz, (c) fc = 0.5Hz, (d) fc = 1Hz.

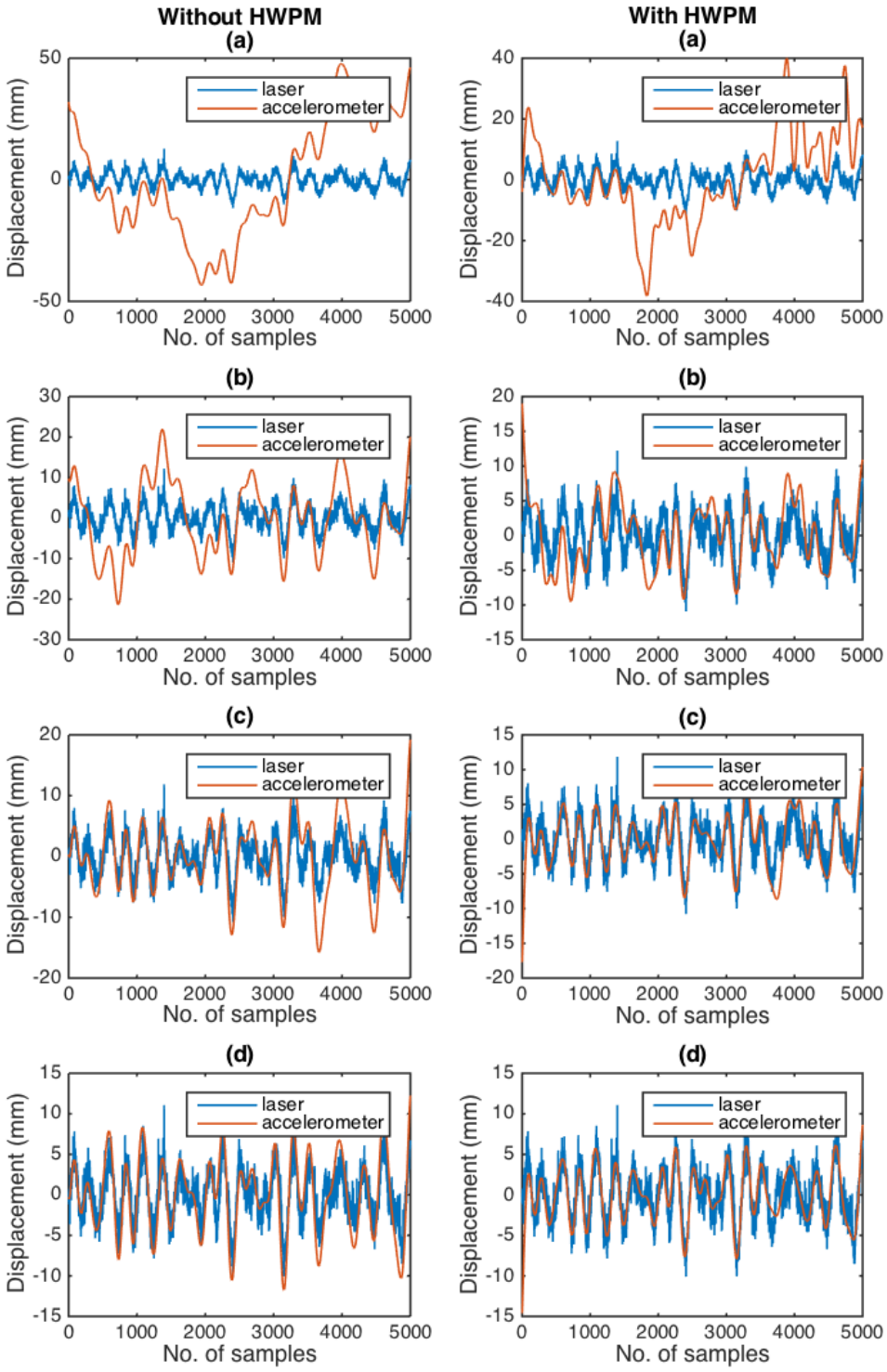

Figure 13: dL and dA samples measured at 50mph to evaluate the drift correction done by HWPM at different cut-off frequencies. (a) fc = 0.1Hz, (b) fc = 0.3Hz, (c) fc = 0.5Hz, (d) fc = 1Hz.

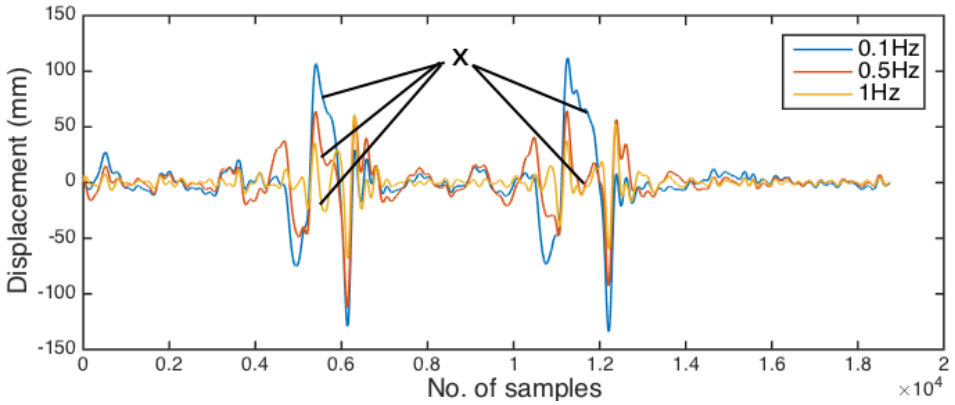

Figure 14 dL sample of a road hump shown at different high-pass filter cut-off frequencies

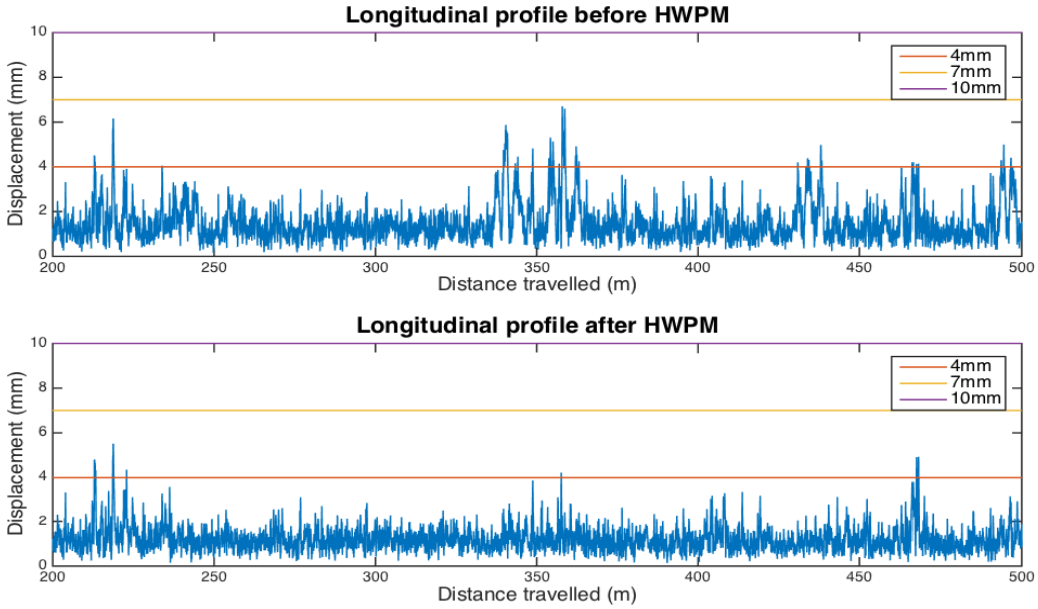

Figure 15: The evaluated longitudinal road profile before and after HWPM, showing the pavement irregularities at thresholds 4, 7 and 10 mm.